Selection of cathode materials for forsterite-supported solid oxide fuel cells – Part II: Electro-catalytic activity

Authors: Fabian Grimm[a]*, Michael Neubert[b], Jürgen Karl[b], Norbert H. Menzler[a], Olivier Guillon[a,c]

[a] Forschungszentrum Jülich GmbH, Institute of Energy and Climate Research, Materials Synthesis and Processing (IEK-1), 52425 Jülich, Germany

[b] Friedrich-Alexander-Universität Erlangen-Nürnberg (FAU) Chair of Energy Process Engineering, 90429 Nürnberg, Germany

[c] JARA-ENERGY, 52425 Jülich, Germany

*f.grimm@fz-juelich.de

Keywords:

- Solid oxide fuel cell
- Forsterite
- Cathode
- Performance
- Electrochemical impedance spectroscopy
- Humidified single-cell tests

Abstract

Based on the interactions and the formation of secondary phases of various SOFC cathode materials if they are processed with the restrictions of an inert-supported cell utilizing forsterite as support material (described in Part I), impedance measurements and cell tests were performed to clarify the impact of the described interactions on the material combinations electrocatalytic performance.

Subsequently Part II focusses on the preselection of a cathode material displaying a higher catalytic activity compared to the currently used LSM/8YSZ cathode of the inert-supported cell concept. In order to do so symmetrical cells, mimicking the processing, were fabricated by co-firing various cathodes ($La_{0.58}Sr_{0.4}Co_{0.2}Fe_{0.8}O_3$; $Pr_{0.58}Sr_{0.4}Co_{0.2}Fe_{0.8}O_3$; $La_{0.58}Sr_{0.4}CoO_3$; $La_{0.58}Sr_{0.4}FeO_3$; $La_{0.58}Ca_{0.4}Co_{0.2}Fe_{0.8}O_3$; $(La_{0.8}Sr_{0.2})_{0.95}Fe_{0.2}Mn_{0.8}O_3$; $(La_{0.9}Sr_{0.1})_{0.95}Fe_{0.7}Mn_{0.3}O_3$) together with an $La_{0.65}Sr_{0.3}MnO_3$ current collector layer (CCL) or with one LSM CCL containing 20 wt% of forsterite.

The results indicate that the catalytic activity of the cathodes cannot simply be related to the number or amount of secondary phases formed during the co-firing if forsterite is present or not as LSF, which displayed the formation of numerous secondary phases (Part I), exhibits the best catalytic activity. The following ascending order of catalytic activity was obtained: LSF (0.25 Ωcm²) > LSM/8YSZ > PSCF > LSFM > LSCF > LCCF > LSC (77.43 Ωcm²).

1 Introduction

An inert-supported-cell (ISC) concept utilizing a low-cost manufacturing route was developed, using magnesium silicate (Mg_2SiO_4) forsterite as support at the air side. Compared to anode and metal supports, forsterite can be classified as a cheap material as its basic oxides are abundant. [1] To even further reduce the manufacturing costs of this ISC, the whole cell is manufactured with a single heat-treatment step at 1100°C<T<1300°C so that the total cell costs can be drastically reduced. To the best of our knowledge, the influence of using forsterite as support material in combination with the above-mentioned low-cost co-firing manufacturing route has not yet been investigated in the literature. Previous work has shown that cathode optimization is necessary to improve the electrochemical performance of this inert magnesium-silicate substrate-supported cell concept. To date, cell performance is rather poor due the formation of Zn–Mn spinel at the triple-phase boundaries (Zn originating from the support, Mn from the cathode) and the impact of co-firing at 1100°C<T<1300°C on the microstructure. [2, 3]

Part I of this paper focusses on the high-temperature stability and reaction tendency of seven cathode materials with forsterite. These properties were crystallographically analyzed by X-ray diffraction (XRD) and optically by SEM. The high-temperature stability was evaluated by pressing cathode raw powder into pellets, sintering them (standard heat treatment program), and analyzing them with respect to their secondary phase formation. The same procedure was applied with respect to the reaction tendency of the cathodes and forsterite by mixing cathode and forsterite powder (weight ratio 1:1) followed by a pressing and sintering step. For phase analysis, the mixed pellets were examined by XRD. These results, discussed in detail in Part I, are summarized in Table 1 and should act as a basis for the electrocatalytic effects presented here in Part II.

Cathode	Heat treatment 1100°C<T<1300°C Formation of secondary phases				
	Pure cathodes	Cathode mixed with forsterite			
LSCF	$SrFeO_{2.8064}$	$Sr_2Mg(Si_2O_7)$	$Sr_2La_8(SiO_4)_6O_2$	$Fe_{1.71}Mg_{1.43}O_4$	
PSCF	Sr_2FeO_4	$Sr_2Mg(Si_2O_7)$	$Sr_2Pr_8(SiO_4)_6O_2$	$Fe_{1.71}Mg_{1.43}O_4$	
LSF		$Sr_2Mg(Si_2O_7)$	$ZnFe_2O_4$	Ca_2SiO_4	SiO_2
LCCF	$LaCo_{0.5}Fe_{0.5}O_3$	$Ca_3Mg(SiO_4)_2$	$CaLa_4(SiO_4)_3O$		
LSFM_95S1M3	$LaFeO_3$	Fe_3O_4	$La_{9.33}(Si_6O_{26})$		
LSFM_95S2M8		La_2O_3	$La_{0.7}Sr_{0.3}FeO_3$		
LSC	$LaCoO_{2.934}$	Sr_2Si	$SrSi_2$	$Co_{1.76}Zn_{13.24}$	

Table 1. XRD results derived from the cathode and cathode mixed with forsterite powders after sintering at 1100°C<T<1300°C. The column "Pure cathodes" lists the secondary phases evolved after heat treatment of the raw cathode material. The column "Cathode mixed with forsterite" displays the secondary phases with are formed after heat-treatment if forsterite is present.

The cathode materials can be classified by electrochemical impedance spectroscopy (EIS), which is the method of choice when the electrode performance of SOFCs is to be evaluated. [4] The cathodes and the influence of the formation of secondary phases, discussed in depth in Part I of this paper (Table 1), can thus be electrochemically analyzed. EIS provides information about the total ohmic resistance and the polarization resistance of a test setup summed up in the obtained Nyquist plot. The ohmic resistance is strongly affected by the EIS device itself and the contacting of the model cell. [4, 5] The polarization resistance (R_{pol}) can be attributed to the oxygen reduction reaction for cathodic symmetrical cells. The polarization is thus affected by the cathode/electrolyte interface. [6]

Furthermore, R_{pol} is influenced by various factors since similar cathode materials, treated in different ways, display varying R_{pol} values.

Leonide et al. [7] identified the influence of different A- and B-site cations on the respective polarization resistance. The authors tested three different compositions by varying the cathode of an ASC with $La_{0.58}Sr_{0.4}Co_{0.2}Fe_{0.8}O_{3-\delta}$, $La_{0.68}Sr_{0.3}Co_{0.2}Fe_{0.8}O_{3-\delta}$ and $La_{0.68}Sr_{0.3}FeO_{3-\delta}$ (cathodes sintered at 1080 °C [8]). The measured polarization resistance at T≈750°C amounts to 0.015, 0.065 and 0.024 Ωcm², respectively. These results show that higher amounts of Sr lead to lower polarization resistances (La58SCF vs La68SCF).

However, the Goldschmidt tolerance factor has to be mentioned in this context. This factor can be used to calculate the deviation of a certain perovskite material from the ideal ABO_3 structure. Meng et al. [9] studied the result of changing the Sr content from x=0.2 to 0.6 of $Pr_{1-x}Sr_xCo_{0.8}Fe_{0.2}O_{3-\delta}$. Increasing the amount of Sr (increased Goldschmidt tolerance factor) results in a change of the valance state of the B-site elements from $^{3+}$ to $^{4+}$ cations. The charge transfer gap thus decreases resulting in a semiconductor to metal transition. However, x=0.4 displayed the lowest R_{pol} values and the highest total conductivity - leading to the conclusion that there is an optimum Sr content (represented by the Goldschmidt tolerance factor) for each perovskite material.

The influence of different A- and B-site elements becomes even more obvious by comparing the results of $La_{0.8}Sr_{0.2}FeO_3$-YSZ and $La_{0.8}Sr_{0.2}MnO_3$-YSZ symmetrical model cells [10] with those obtained by Leonide et al. [7] After sintering the cathodes at 1200°C, Kong et al. [10] obtained R_{pol} values at 800 °C of 0.24 and 0.3 Ωcm², which are ten times higher than the values obtained by Leonide et al. [7] As this huge difference may not only be due to the difference in amounts of Sr (0.3 vs 0.2), the higher sintering temperature (1200 °C instead of 1080 °C [8]) may not have negligible effects.

This assumption is underlined by the findings of Wang et al. [11] The authors sintered different cathodes such as $La_{0.8}Sr_{0.2}FeO_3$-YSZ, $La_{0.8}Sr_{0.2}CoO_3$-YSZ and $La_{0.8}Sr_{0.2}MnO_3$-YSZ at 1250 °C on Anode Supported Cells and measured the R_{pol} at 700 °C. The R_{pol} amounted to

0.35 Ωcm², 0.15 Ωcm² and 0.65 Ωcm², respectively. These values are slightly higher than that measured by Kong et al. [10] (0.35 Ωcm² LSF sintered at 1250 °C vs 0.24 Ωcm² for LSF sintered at 1200 °C) indicating the influence on the R_{pol} by the cathode sintering temperature. In order to verify this, Wang et al. [12] varied the firing temperature of LSF-YSZ cathodes on ASCs from 850 °C to 1100 °C and measured an increase in polarization resistance from 0.3 Ωcm² to 0.93 Ωcm². As no solid-state reaction between LSF and YSZ was detectable at 1100 °C, the authors related the increase in R_{pol} to the loss of TPB due to the much denser LSF-YSZ cathode. A similar result was obtained by the group of Meng et al. [9] The authors varied the sintering temperature of $Pr_{0.6}Sr_{0.4}Co_{0.8}Fe_{0.2}O_{3-\delta}$ with gadolinium-doped ceria (GDC) model cells from 950 °C to 1050 °C and noted an increase in the Rpol at 800 °C from 0.05 to 0.516 Ωcm², which represents an increase of more than a factor of ten.

Furthermore, the preparation route of the respective cathode material influences the measured R_{pol}. Guo et al. [13] studied the impact of the synthesis route of $Pr_{0.6}Sr_{0.4}Co_{0.2}Fe_{0.8}O_{3-\delta}$ on the R_{pol} by comparing an acetic acid–hexamethylenetetramine and an EDTA-citric acid synthesis route. After sintering the PSCF cathode at 1050°C, the PSCF obtained from the EDTA-citric acid route displayed an R_{pol} of 0.64 Ωcm² at 600°C which is 30% larger than the R_{pol} of 0.45 Ωcm² of the PSCF derived via the amine route. The authors mainly explain this result by the difference in particle size and thus the influence of the cathode microstructure as the PSCF achieved via the amine route provides a larger surface area. Similar results were obtained by Zhao et al. [14]. The authors compared three LSC samaria-doped ceria (SDC) model cell types by varying the preparation of the cathode: impregnated LSC-SDC, screen-printed LSC-SDC and screen-printed LSC. All three samples were fired at 950°C and analyzed by impedance spectroscopy. The results obtained at 750°C indicate R_{pol} values of 0.06, 0.16 and 0.95 Ωcm² mainly originating from the differences in active catalytic surface area due to the variation in the preparation route of the three model cells.

To summarize these findings, the cathodic R_{pol} is influenced by the microstructure and the chemical composition. The microstructure is affected by the raw powders in terms of particle-size distribution and particle shape. The packing density finally obtained can therefore be influenced by varying the manufacturing and sintering conditions. In addition, these factors are also influenced by the chemical composition [15] of the cathode as the number of oxygen vacancies influences the ionic conductivity [16], and the type and combination of A-site and B-site elements influence physical parameters such as electron conductivity, electron hopping mechanism and coefficient of thermal expansion [16, 17]. Furthermore, the chemical composition also influences the sinterability [15] and thereby affects the final density, specific surface area and the particle size.

Summarizing Part I, only LSFM_95S2M8 and LSF displayed a stable behavior at the 1100 °C<T<1300 °C sintering conditions. The conclusion was that the decomposition of the cathodes promote the reaction with forsterite ending up with the following ascending order of cathode reaction tendency: LSFM (both stoichiometries) > LSF > LSC > PSCF > LSCF > LCCF.

As part of this work, the effects of forsterite as support material and co-sintering at 1100 °C<T<1300 °C on the cathode microstructure were studied by measuring R_{pol} of the model cells. The aim of this work is to link the cathode-forsterite reaction tendency with the R_{pol} obtained from EIS, and thus to finally recommend a cathode material with good performance for the forsterite-supported cell. In order to do so, two different symmetrical cells were prepared. One setup utilizes pure LSM as the current collector layer (CCL), the second one uses a mixed LSM CCL (20 wt% forsterite was added), hence visualizing, in terms of changing the R_{pol} values, the impact of contact with forsterite. These layers were then co-fired applying the standard heat treatment at 1100 °C<T<1300 °C to mimic the low-cost manufacturing route. The cathode with the lowest R_{pol} value was chosen for single-cell tests and to monitor the degradation of the cathode under humidified and dry air conditions.

2 Experimental

Seven different cathode materials were subsequently investigated with respect to their high-temperature stability, reaction tendency with forsterite and electrochemical performance revealed by the EIS measurements.

The seven cathode materials are: LSCF ($La_{0.58}Sr_{0.4}Co_{0.2}Fe_{0.8}O_3$), LSC ($La_{0.58}Sr_{0.4}CoO_3$), LSF ($La_{0.58}Sr_{0.4}FeO_3$), PSCF ($Pr_{0.58}Sr_{0.4}Co_{0.2}Fe_{0.8}O_3$), LCCF ($La_{0.58}Ca_{0.4}Co_{0.2}Fe_{0.8}O_3$), LSFM 95S1M3 ($(La_{0.9}Sr_{0.1})_{0.95}Fe_{0.7}Mn_{0.3}O_3$), and LSFM 95S2M8 ($(La_{0.8}Sr_{0.2})_{0.95}Fe_{0.2}Mn_{0.8}O_3$). The synthesis routes and powder properties are described more in detail in Part I. LSCF (with an A-site sub-stoichiometry) is currently the state-of-the-art cathode material in various SOFC applications. LSC and LSF were chosen to be able to analyze the influence of the respective B-site perovskite elements. PSCF and LCCF indicate the influence of a different A-site element with respect to LSCF. The two LSFM compositions represent a variation of the currently used LSM/8YSZ cathode material in terms of the amount of manganese. LSCF, LSC, LSF and PSCF were synthesized in-house via the spray pyrolysis route. LSFM 95S1M3, LSFM 95S2M8 and LCCF were synthesized by the Pechini method. To exclude possible influences of different particle sizes, the difference of the d_{10}, d_{50} and d_{90} was kept as small as possible among the seven cathode inks. The properties of the cathode inks (consisting of 62.75 wt% cathode material, 20.85 wt% terpineol (DuPont) and 16.4 wt% of a transport medium composed of 6 wt% of 45 cp ethyl cellulose and terpineol) are listed in Table 2

Cathode	Particle size			Viscosity
	d_{10}	d_{50}	d_{90}	
	[µm]	[µm]	[µm]	[Pa·s]
LSCF	0.63	0.88	1.21	22.9
PSCF	0.60	0.82	1.10	13.4
LSC	0.61	0.85	1.16	12.7
LSF	0.58	0.77	1.00	13.8
LSFM 95S1M3	0.61	0.88	1.26	11
LSFM 95S2M8	0.60	0.79	1.05	13.8
LCCF	0.40	0.80	2.48	13.3

Table 2. Properties of the different cathode inks which were screen printed on the 8YSZ-GDC model cells for the EIS measurements. The viscosity was measured at a shear rate of 109 s^{-1}. All values are rounded to the second decimal place.

The different cathode materials were subjected to EIS measurements, from which the Nyquist plot can be obtained. The ohmic resistance (R_{ohm}) and polarization resistance (R_{pol}) can be derived from the Nyquist plot as shown in Figure 1.

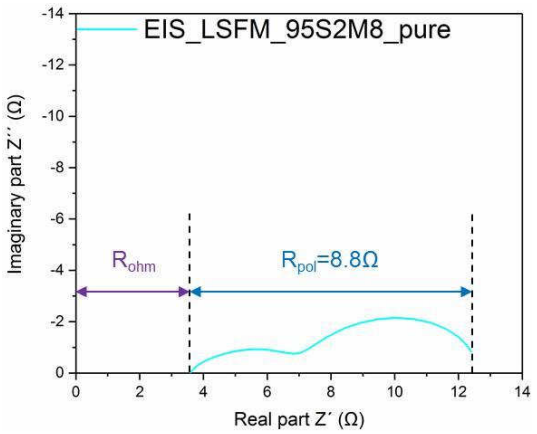

Figure 1: Nyquist plot of the EIS_LSFM_95S2M8_pure sample. The graph can be subdivided into the ohmic part (R_{ohm}) and the polarization resistance (R_{pol}).

R_{ohm} is, for instance, affected by the device itself and by the type, quality and material with which the sample is contacted. To eliminate these factors only R_{pol} was considered.

Therefore, to underline the difference in the R_{pol} values, R_{ohm} was subtracted in the EIS measurements. By doing so, EIS offers the opportunity to visualize, in terms of R_{pol} values, the influence of the formation of secondary phases –irrespective of whether they evolve due to reactions with forsterite or cathode decomposition – as well as the impact of the low-cost co-firing manufacturing route (in terms of microstructural changes and co-firing capability of the cathode materials), thereby allowing cathode benchmarking.

In order to do so, two symmetrical cell setups were prepared. 8YSZ (200µm; Kerafol, Marktredwitz, Germany) was used, screen-printed with a GDC barrier layer with a wet-layer thickness (WLT) of 35 µm, which was sintered at 1300°C for 3h under air. A current collector layer (CCL), consisting of 50 wt% $La_{0.65}Sr_{0.3}MnO_3$ (LSM) and 50 wt% transport medium (the same as that used for the cathode ink) was subsequently applied after the cathode ink for "pure" samples, and a CCL consisting of LSM and 20 wt% forsterite powder for "mixed" samples was screen printed (D=12mm; WLT=65µm and 2x173µm, respectively). Both sample types were then sintered by the standard sinter process 1100°C<T<1300°C for 5h in air. The symmetrical cell setups are shown schematically in Figure 2. The samples are termed EIS_cathode_pure and EIS_cathode_mixed.

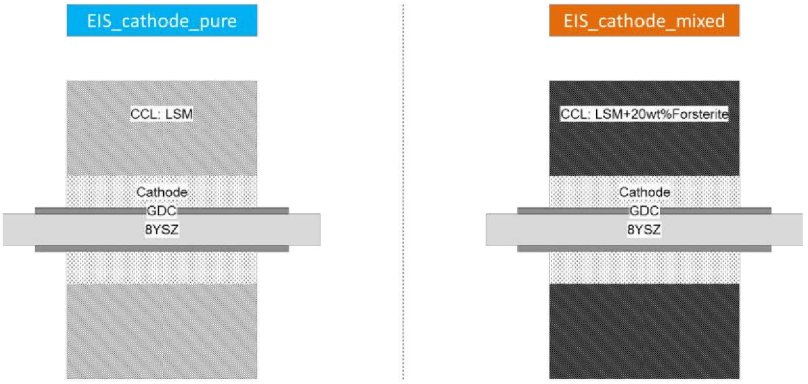

Figure 2: Symmetrical cell design for the samples with a pure LSM CCL (EIS_cathode_pure) and mixed LSM+20 wt% forsterite CCL (EIS_cathode_mixed).

Cross sections of the EIS_cathode_pure and EIS_cathode_mixed samples were obtained by embedding them in epoxy, then grinding and polishing them with silica suspension. The specimens were sputtered with platinum to ensure sufficient electrical conductivity for investigations with a scanning electron microscope (SEM) (Zeiss Ultra55 with EDX from Oxford Instruments; INCAEnergy400 and Feico Phenom). The pore volume quantification was performed for each cathode material with the "Analysis Pro" software from Olympus. The mean values of five images per cathode were considered.

For single-cell tests ESC (sintered) substrates provided by Kerafol were used. The ESC utilizes a NiO/GDC anode, a 90µm 3YSZ electrolyte and a GDC barrier layer. An LSF cathode layer (2x2cm; 65µm WLT) and two LSM CCL for "pure" samples and two LSM CCL consisting of LSM and 20 wt% forsterite powder for "mixed" samples (2x2cm, each with a WLT of 178µm) were screen-printed on top of the GDC layer and then co-fired at 1100°C<T<1300°C. The cells were contacted by a nickel mesh at the anodic side and a gold mesh on the cathodic side. The device itself was made in-house. The total setup was manufactured out of Al_2O_3 – including the cell housing and the gas distribution pipes. To ensure gastight sealing, the cell was pressed onto the nickel mesh with a defined Al_2O_3

weight and an alumina plate applied acting as height adjustment to avoid leakages. Additionally, the cell was surrounded with an Al_2O_3 frame providing the required gas tightness.

The single-cell tests were performed with humidified air (at T=60°C) and dry pressurized air (3Nl/min) at the cathode side and 0.3Nl/min of H_2 and N_2 (total volume flux of 0.6Nl/min) at a cell temperature of 750°C. Furthermore, galvanostatic (0.125 A/cm²) degradation tests were performed while the cell voltage (U_{Cell}) was monitored for 24h. Switching the feed gas of the cathode between humidified and dry pressurized air enabled the influence of water vapor at the cathodic side to be visualized. The cathodic gas was humidified by bubbling the pressurized air through a water bottle filled with demineralized water. A maximum humidification level of 130 g/m³ was achieved by heating the water to 60°C (saturated air). The gas pipe from the bottle to the device was heated to avoid water condensation. The impact of the humidified and dry air on the cathode microstructure was studied on cross sections prepared in the same way as the EIS_cathode samples.

In summary, four different sample types were prepared and analyzed:

I. EIS_cathode_pure:
   Cathode ink and LSM CCL screen-printed on sintered 8YSZ+GDC and sintered with the standard heat-treatment program
II. EIS_cathode_mixed:
   Cathode ink and LSM+20 wt% forsterite CCL screen-printed on sintered 8YSZ+GDC and sintered with the standard heat-treatment program

Based on the results from samples I and II only LSF was selected as the cathode material for sample III and IV, since in these tests LSF displayed the best results

III. ESC_LSF_pure

LSF ink and LSM CCL were screen-printed on an already sintered ESC (Kerafol). The ESC had a NiO / GDC anode, a 90µm 3YSZ electrolyte and a GDC barrier layer.

IV. ESC_LSF_mixed

LSF ink and LSM+20 wt% forsterite CCL were screen-printed on an already sintered ESC (Kerafol). The ESC had a NiO / GDC anode, a 90µm 3YSZ electrolyte and a GDC barrier layer.

3 Results

Seven different cathode materials were examined with respect to their electrocatalytic activity, microstructure and stability. These cathode materials, their reactivity with the support material forsterite (investigated by XRD, SEM and EDX measurements) are described in detail in Part I of this paper. The currently used LSM/8YSZ cathode of the forsterite ISC concept is added as the reference cathode for the impedance measurements.

3.1 Electrochemical impedance measurements

EIS was used to measure the performance of each cathode material in terms of the respective polarization resistance. Low polarization resistance (R_{pol}) values therefore indicate a cathode that performs well. A cathode suitable for the low-cost co-firing manufacturing route and additionally displaying good performance while in contact with forsterite or not was sought. Therefore, symmetrical cell setups were prepared for each cathode material (cf. Figure 2). By comparing the “pure” and “mixed” setups, it was possible to visualize the impact of the formation of secondary phases with forsterite. Note that in the real ISC the forsterite is in direct contact with the CCL and mixing the forsterite with the cathode material leads to a poorer result as the contact area between the two phases is enlarged.

As described in the experimental section, only R_{pol} was considered for benchmarking the cathode materials. Therefore, to underline the difference in the R_{pol} values, R_{ohm} is subtracted, as shown in Figure 3.

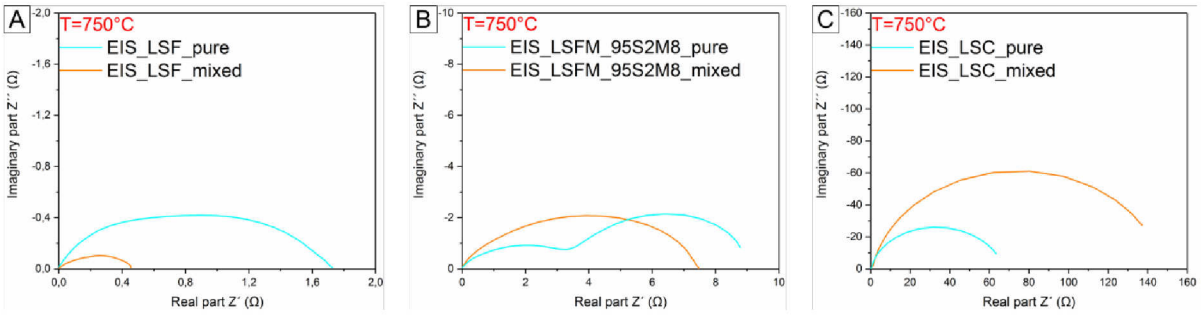

Figure 3: Nyquist plots of the EIS_cathode_pure (blue) and EIS_cathode_mixed (orange) samples at T=750 °C for the cathodes (A) LSF; (B) LSFM_95S2M8 and (C) LSC. Note the differences in the scaling of the x-axis. The Nyquist plots of the other cathodes are listed in Supplementary 1.

Figure 4 shows R_{pol} values for EIS_LSF of 1.73 Ω (pure) and 0.45 Ω (mixed). The same trend, i.e. that the samples with a "mixed" CCL display a slightly lower R_{pol} value, can be obtained for LSFM_95S2M8 with 8.79 Ω (pure) compared to 7.46 Ω (mixed). LSC displays the expected trend: i.e. higher R_{pol} values for the mixed samples: 63.44 Ω (pure) and 137.15 Ω (mixed).The R_{pol} values can then be related to the active surface area of the sample (D=12mm; A=1.1cm²) by applying the following formula: R_{pol} (Ω) * A/2 (cm²) = $R_{pol;area}$ (Ωcm²). These $R_{pol;area}$ values are listed in Figure 4 for all of the examined cathodes, plus the reference sample LSM/8YSZ.

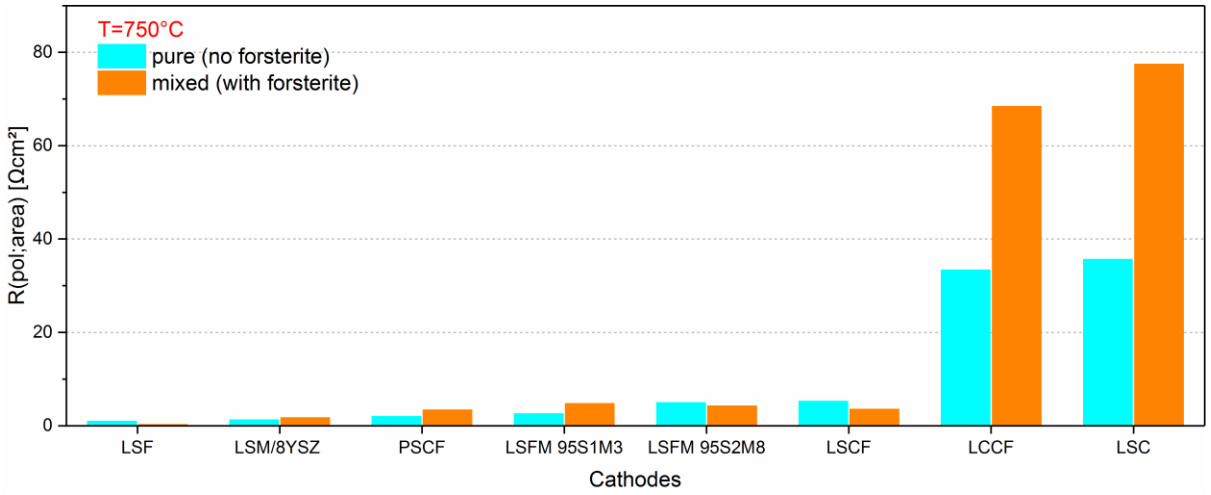

Figure 4: Bar chart of the $R_{(pol;area)}$ values for the EIS_cathode_pure and EIS_cathode_mixed samples. LSM/8YSZ is the cathode material currently used for the ISC.

Figure 4 shows that LSF can be regarded as the best-performing cathode irrespective of whether the CCL is pure or mixed with forsterite: $R_{(pol;area)}$ values of 0.96 (pure) and 0.25 (mixed) Ωcm² were obtained. LSC displays the highest $R_{(pol;area)}$ values with pure and mixed values of 35.61 (pure) and 77.43 (mixed) Ωcm². LSFM_95S2M8 occupies an intermediate position displaying moderate (in comparison with the LSF and LSC values) $R_{(pol;area)}$ values with 4.96 (pure) and 4.24 (mixed) Ωcm².

With respect to the interaction tests of the above-mentioned cathodes with forsterite in Part I of this paper, these results indicate that the formation of secondary phases due to contact with forsterite does not correlate with the measured $R_{(pol;area)}$ values. Otherwise LSF would have been expected to show $R_{(pol;area)}$ values in the same order of magnitude as LSC (as both display a strong reactivity with forsterite) and LSFM_95S2M8 to show significantly lower $R_{(pol;area)}$ values (as its reaction tendency with forsterite is limited).

3.2 Cross-section characterization of EIS_cathode

In order to obtain more insights into the huge differences within the measured $R_{(pol;area)}$ values of the cathode materials, cross sections of each EIS_cathode sample were prepared after performing the EIS measurements.

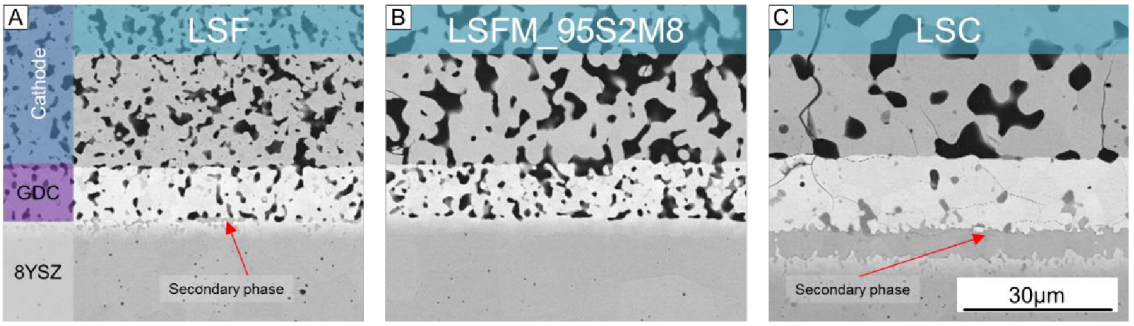

Figure 5: Cross sections of the EIS samples: 8YSZ (grey) + GDC barrier-layer (purple) substrates with different cathode layers (blue): (A) LSF, (B) LSFM_95S2M8 and (C) LSC.

In direct comparison, Figure 5 shows three observable global differences which can be described as follows:

I. Cathode densification

The EIS_LSC sample (Figure 5 (C)) displays a much denser (17.8 vol% porosity) cathode layer compared to the EIS_LSFM_95S2M8 (40.7 vol% porosity) and EIS_LSF (33.5 vol% porosity) samples. As the particle size of the cathodic inks was kept constant (focus on the respective $d_{(50)}$ value; cf. Part I of this paper), this result highlights the difference in the sinterability of the utilized materials. From the literature, it is known that the electrocatalytically active surface area has a drastic impact on the $R_{(pol;area)}$. [13]

II. GDC densification

Comparing the three different samples in Figure 5, only the sample which utilizes LSC as the cathodic layer (EIS_LSC; Figure 5 (C)) displays GDC post-densification by cathode sintering. To obtain more insights, the EIS_LSF (representative of a porous GDC layer) and EIS_LSC samples (representative of the GDC densification) were compared with SEM-EDX measurements (Figure 6).

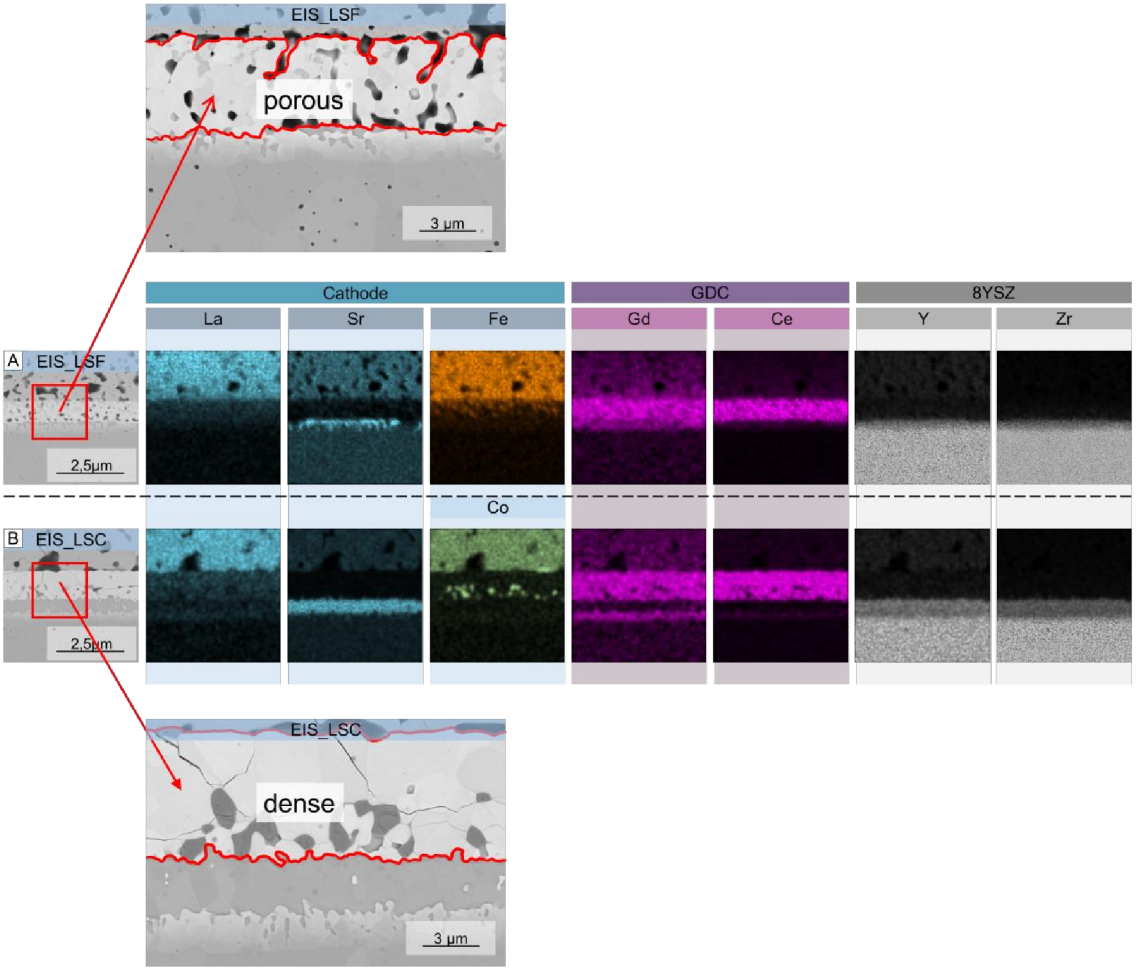

Figure 6: EDX mapping of the EIS samples with (A) LSF and (B) LSC as the cathodic layer. The brightness is correlated with the concentration of the elements. Regions appearing as black do not contain any traces of the respective element

The only difference in the EIS_LSF and EIS_LSC samples (Figure 6 (A) and (B)) is the B-site cation: Fe vs. Co. Notably for EIS_LSC, a denser GDC layer can be observed (highlighted with the zoomed SEM picture of both samples in Figure 6, surrounded by a red line). This densification of GDC was systematically studied for all the cathodes listed in Table 2, mixed with forsterite and pure, and was only observed for the samples with LSCF, PSCF, LCCF or LSC as the cathode layer (irrespective of pure or mixed CCLs).It therefore appears that Co may be responsible for the observable densification of GDC. (cf. Supplementary 2).

III. Secondary phase formation beneath the GDC layer

As already visible in Figure 5, EIS_LSF and EIS_LSC display the formation of a secondary phase beneath the GDC layer (Figure 5 - red arrows). To an even greater extent, Figure 6 highlights the secondary phase formation with the SEM pictures and EDX mappings of these samples. The EDX mapping (Figure 6) displays a Sr and Zr accumulation beneath the GDC layer. Additional EDX point scans support these findings as the secondary phase formation could be related to a Sr-Zr-O-rich phase. Only the two samples EIS_LSFM_95S1M3 and EIS_LSFM_95S2M8 did not display any secondary phase formation beneath the GDC layer. With respect to the other samples, a correlation was established between Sr-Zr-O and Ca-Zr-O formations displayed in Figure 7 and their respective $R_{(pol;area)}$ values.

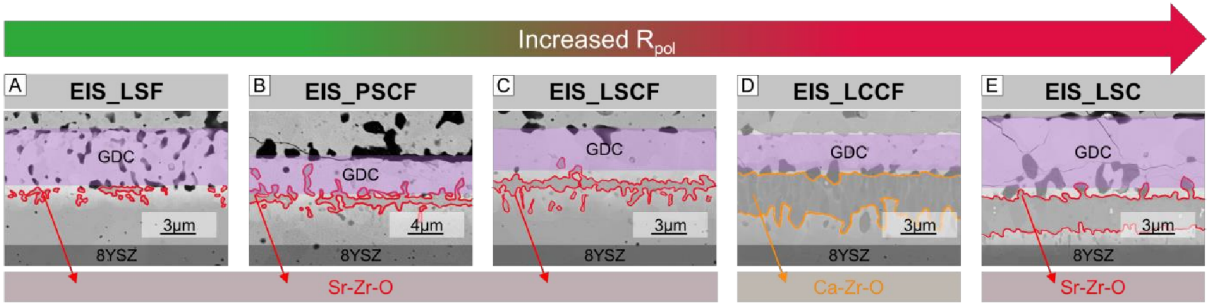

Figure 7: Cross sections of the EIS samples with different cathode layers: (A) LSF, (B) PSCF, (C) LSCF, (D) LCCF and (E) LSC.

Figure 7 displays the symmetrical cells in ascending order of their $R_{(pol;area)}$ values starting with the lowest $R_{(pol;area)}$ values (LSF) and proceeding to the highest $R_{(pol;area)}$ values (LSC). The secondary phase formation of Sr-Zr-O (highlighted in red) and Ca-Zr-O (highlighted in orange) was analyzed by EDX point scans and EDX mappings. It is assumed that these phases refer to $SrZrO_3$ and $Ca_{0.15}Zr_{0.85}O_{1.85}$. In the literature, these phases are known to be electrically insulating [18-20]. Notably, the $R_{(pol;area)}$ values correlate with the formation of the secondary phase beneath the GDC layer. It seems that a continuous Sr-Zr-O or Ca-Zr-O layer drastically affects the $R_{(pol;area)}$. Bearing this in mind while comparing the samples with LSF, PSCF and LSCF as the cathodic layer (Figure 7 (A), (B) and (C)), it is reasonable to assume that the sample with LSCF displays a higher $R_{(pol;area)}$ value compared to EIS_PSCF and EIS_LSF as a continuous Sr-Zr-O for EIS_LSCF is observable. Furthermore, this assumption is supported by EIS_LSF and EIS_LSC. EIS_LSF only displays island-like secondary Sr-Zr-O phases. In contrast, EIS_LSC evolves a continuous and ≈3µm thick Sr-Zr-O layer.

3.3 *Single-cell tests*

As EIS_LSF_pure and EIS_LSF_mixed displayed the lowest $R_{(pol;area)}$ values, LSF was used as the cathode material for single-cell tests.

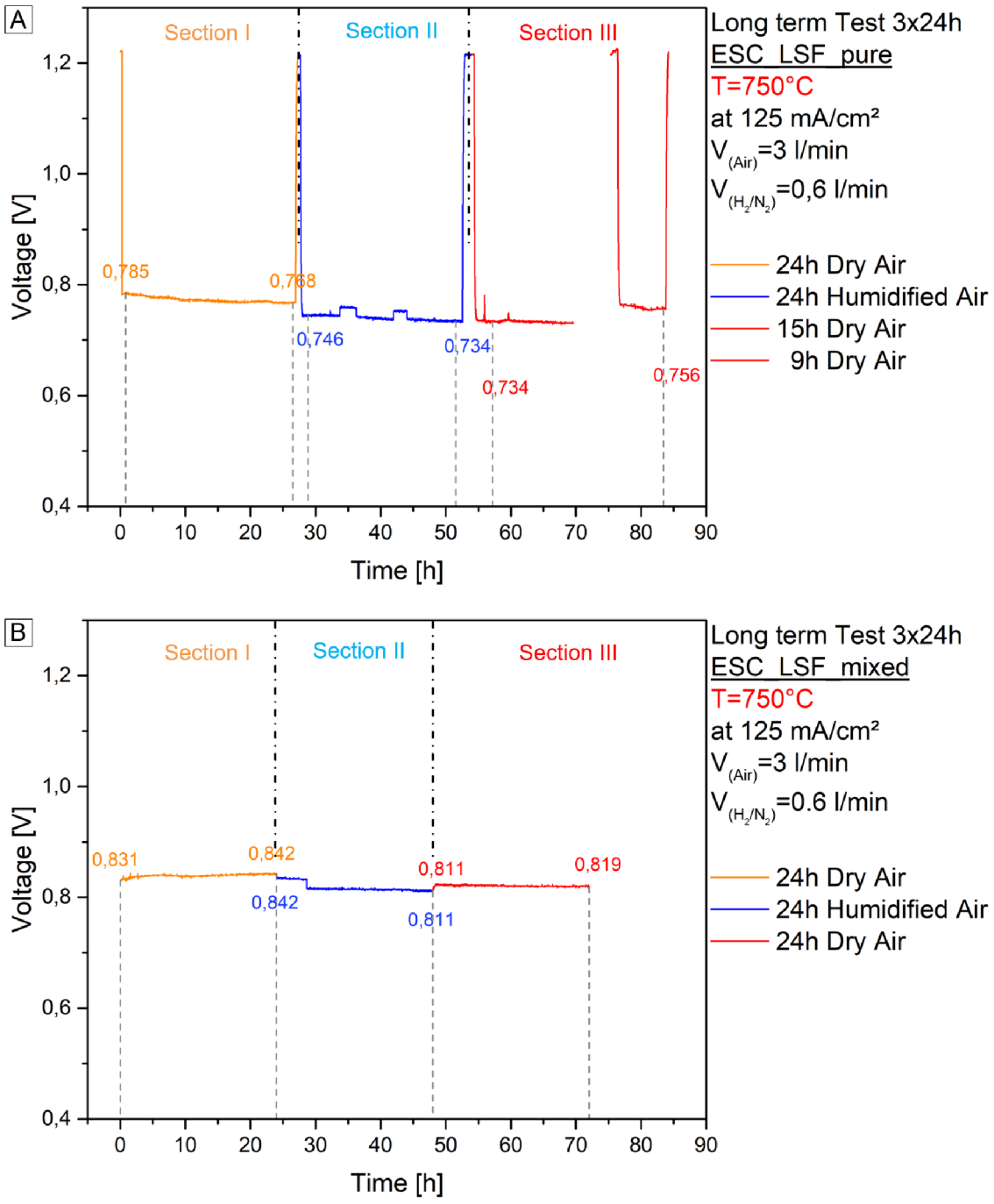

Figure 8: Galvanostatic single-cell tests of an ESC with LSF as cathode and an (A) LSM CCL "pure" layer and an (B) LSM CCL "mixed" layer. T=750°C; I=125 mA/cm²; t=3x24h. The V-I curve was measured before and after each test for ESC_LSF_pure. In Section I the cell was fed with dry air, in Section II with humidified air (water bubbler t=60°C; 3l/min) and in Section III the cell was fed again with dry air.

For the ESC_LSF_pure (Figure 8 (A)) the cell displays a degradation from 785 mV to 768 mV, which amounts to a loss of 2.2% (degradation of 0.65 mV/h), in section I (dry air). Switching from dry air to humidified air in Section II leads to an initial drop of the voltage from 768 mV to 746 mV, which at 734 mV is even more strongly pronounced after 24 h. In total, air humidification doubles (with respect to Section I) the observable degradation effect to a loss of 1.56 mV/h. Interestingly, Section III starts with the same value of 734 mV indicating that the degradation is not reversible. After 7h of operation, in Section III the device (oven and power supply) broke down leading to a temperature drop from 750°C to 600°C while the cell was flushed with dry air in OCV mode. After restarting the measurement (the cell was flushed with dry air for 9h at 600°C) the voltage at a current density of 125 mA/cm² displayed 756 mV and thus an increase of 2.2% compared to the initial 734mV of Section III. Compared to that the ESC_LSF_mixed (Figure 8 (B)) displayed in section I (dry air) an increase from 831 mV to 842 mV, which amounts to a plus of 1,3 % (increase of 0.46 mV/h). Switching to humidified air leads after a short delay of 4 h to a drop of the cell voltage from 842 mV to 811 mV (loss of 1.29 mV/h). Switching back to dry air (section III) leads again to a slow increase of the cell voltage from 811 mV to 819 mV (increase of 0.33 mV/h).

Both cells, whether with or without forsterite, display an increase of the cell voltage if switching from humidified air (section II) to dry air (section III). These results indicate that only one part of the cathode may be degraded as the initial performance could be partially restored for both cell setups. Nevertheless, in total with 785 mV / 831 mV as the initial and 756 mV / 819 mV as the final value, the cells displayed a total loss of 3.7 % (degradation of 0.35 mV/h) for the ESC_LSF_pure and a total loss of 1.4 % (degradation of 0.16 mV/h) for the ESC_LSF_mixed setup.

4 Discussion

The results of this study can be summarized in three major parts:

Densification of GDC

In the literature [21] , GDC post-densification was observed after sintering LSCF on a GDC layer, relating this effect to the presence of Fe, Sr and Co in the GDC layer. However, due to the screening of several cathodes, listed in Table 2Table 1, it was possible to exclude each element regarded in the literature as responsible for the densification of GDC. The GDC densification was only observed for LSCF, LSC, PSCF and LCCF. As LSC has no iron in the structure and LCCF no strontium, the only conclusion could be that cobalt is responsible for the observed GDC densification. That fact is strongly supported by Jud et al. [22], pointing out that GDC doped with 1mol% of CoO displays enhanced densification rates compared to pure GDC.

This conclusion correlates with the phase stability of the examined cathodes and the recorded volatility of Co (in Part I of this paper) in the temperature range of 1100°C<T<1300°C. Table 1 shows that none of the cathodes containing Co are stable at high temperature and evolve secondary phases after heat treatment.

Electrocatalytic activity

The electrocatalytic activity examined by EIS measurements is influenced by three main factors:

- High-temperature stability of the cathodes:

  A decomposition of the perovskite at high temperatures will result in a change of its catalytic properties. LSC and LSCF are commonly known to display low polarization resistance. In the literature, values of 0.01 Ωcm^{-2} at T=750°C for LSC [23] and LSCF

[24] can be found. In contrast, the present study revealed very high polarization resistances of 35.61 Ωcm^{-2} for LSC (pure) and 5.27 Ωcm^{-2} for LSCF (pure) at T=750°C after co-firing the symmetrical cells in the temperature regime of 1100°C<T<1300°C. However, even after co-firing at high temperatures, LSF (pure) displays $R_{(pol;area)}$ values of 0.96 Ωcm^{-2}, which are in the same range as that found in the literature (0.35 Ωcm^{-2} at T=700°C [25]). The XRD measurements listed in Table 1 reveal that LSF is stable in the temperature regime of 1100°C<T<1300°C whereas LSC and LSCF are not. The decomposition of LSC and LSCF, by forming secondary phases which refer to $LaCoO_{2.934}$ and $SrFeO_{2.8064,}$ influence the polarization resistance. As the sintering is performed at significant higher temperatures (1100°C<T<1300°C; 5h) compared to the EIS measurement (750°C; 1h) we do not expect any drastic further decomposition of the cathode material during EIS operation. For $LaCoO_3$, the secondary phase formed after the treatment of LSC displays a total conductivity of 0.12 Scm^{-1} at T=500°C [26], which is several factors lower compared to pure LSC (≈1000 Scm^{-1} at T=1000°C [27]).

With respect to $SrFeO_{3-\delta,}$ the secondary phase evolving from LSCF, total conductivity values of 1.5-2 Scm^{-1} can be found in the literature (at 800-1600K) [28]. These values are significantly lower compared to pure LSCF (≈360 – 340 Scm^{-1} at 600-800°C, [29]). These differences in the respective total conductivity values of the secondary phases and the pure perovskite phases underline the significant impact of the decomposition of the cathode materials.

The polarization resistance is affected even more strongly if the current collector is mixed with forsterite due to the formation of additional secondary phases.

- The formation of Sr-Zr-O and Ca-Zr-O correlates with the high-T stability of the cathodes. LSF and LSFM are high-temperature stable (e.g. Table 1). The other cathodes start to decompose at high temperatures, thereby giving easily an excess of Sr and Ca to form the insulating phases $SrZrO_3$ and $Ca_{0.15}Zr_{0.85}O_{1.85}$. These insulating phases affect the polarization resistance. This assumption was validated

very recently by Szász et al. [21], pointing out that $SrZrO_3$ does not only affect the R_{Ohm}, but also $R_{(pol;area)}$ due to the processes associated with $SrZrO_3$ (blocking of oxygen-ion transport) which occurs within the frequency range of cathode polarization. Furthermore, double-layer capacitances at the GDC/$SrZrO_3$ interface, as explained in literature by Szász et al. [21], might be additional reasons. In this respect, the continuity of the insulting layers plays a crucial role. In the literature, a $SrZrO_3$ layer continuity of >95% is reported to have a critical impact upon the R_{pol}. [20, 21] These results correspond perfectly to the findings of the present study. If there is no continuous $SrZrO_3$ layer the effect on the R_{pol} is minimal: for (A) LSF, Figure 7 displays an island-like Sr-Zr-O formation and the lowest $R_{(pol;area)}$ values. If the coverage reaches a critical value, the $R_{pol;area}$ value is significantly increased. This behavior is perfectly represented by the EIS samples from Figure 7 (B) PSCF and (C) LSCF, as for PSCF a nearly continuous and for LSCF a continuous $SrZrO_3$ layer can be obtained. The total conductivities of these perovskites are in the same range at 166 Scm^{-1} for PSCF (T=900°C;1bar p_{O2}; [30]) and 290 Scm^{-1} for LSCF. However, the measured $R_{(pol;area)}$ values for LSCF are more than 2.5 times greater compared to PSCF (5.27 Ωcm^2 vs 1.95 Ωcm^2 for LSCF and PSCF pure samples). Based on the total conductivity values, LSCF would have been expected to display a lower $R_{pol;area}$ value compared to PSCF. This is not the case as for (C) LSCF Figure 7 shows a continuous $SrZrO_3$ layer and for (B) PSCF the layer is only close to continuous. As a conclusion: a continuous $SrZrO_3$ layer drastically increases the polarization resistance.

Single-cell tests:

Nielsen and Mogensen [6] carried out degradation tests on anode-supported cells with an LSM/8YSZ cathode and compared the results with an LSCF/CGO cathode. The authors operated the cell at 750°C with a current density of 410 mA/cm², 10% oxygen and fuel

utilization, and 33% humidified fuel gas. The humidification level at the cathodic side was varied from dry to 6.4 and 12.8 mol%. The authors reported that LSCF/CGO did not show any observable degradation effect. However, LSM/8YSZ displayed a strong influence on the humidification level: at 12.8 mol% humidified air the voltage dropped from 748 mV to 718 mV (amounting to a loss of 4 %) after 24h of operation (-1.25 mV/h). After 120 h, the authors observed a voltage of 680 mV (-0.32 mV/h) then by switching to dry air the voltage slowly increased by 2.8% to 700 mV. After another ≈70h of operation under dry air, the cell reached 710mV. The total loss (initial 775 mV) amounts to 8.4% (0.01 mV/h). It should be noted that this cell test was operated for 735h. The authors' hypothesis is that LSM starts to decompose by displaying an enrichment of the redox active species Mn^{2+} of the cathode material LSM. Mn^{2+} then reacts with H_2O by forming a volatile metal oxide species (e.g. Sr and H_2O react with the formation of $Sr(OH)_2$). As this species is gaseous, the removal of Mn^{2+} is not reversible. These findings are supported by Nielsen, Hagen and Liu [31], who observed the same trend during humidification of cathodic air gas i.e. a partly recoverable degradation of the LSM/8YSZ cathode material if subjected to humidified and then dry air. The authors therefore concluded that the level of humidification plays a crucial role. [31]

This hypothesis describes very well the observable trend which can be derived from Figure 8: after switching from Section I (dry air) to Section II (humidified air) the voltage displays a sharp drop from 768 mV to 746 mV for ESC_LSF_pure (Figure 8 (A)) and from 842 mV to 811 mV for ESC_LSF_mixed (Figure 8 (B)). This behavior is similar to that described in the literature [6]. Furthermore, the initial cell voltage (785 mV / 831 mV for ESC_LSF_pure / ESC_LSF_mixed) was partly restored with a voltage of 756 mV / 819 mV (for Figure 8 (A) / (B)) after switching to Section III (dry air). The overall loss amounts to 3.7% for the cell utilizing a pure LSM CCL layer and to an overall loss of 1.4 % for the ESC_LSF_mixed setup, which is only about half of that reported by Nielsen and Mogensen [6]. As an explanation, the cathode material itself and the manufacturing route of the ESC_LSF_pure cell must be taken into account.

a) The cathodic side consists of LSF and LSM, whereby LSF fulfills the role of the cathode and LSM acts as the CCL. In the literature, LSF is described as stable cathode material [32], in contrast, LSM is known to display a certain Mn depletion during long-term operation [33]. Based on the findings reported in literature, it is apparent that elements out of LSM will most probably tend to form the above-mentioned volatile oxide species in the presence of water. To prove that FactSage calculations with the basic oxides La_2O_3, SrO, Fe_2O_3 and Mn_2O_3 and the presence of water (the amount of H_2O was varied from 3 up to 17 mol%) were performed at 750°C for the ESC_LSF_pure setup. The same FactSage calculations were additional performed with the basic oxides MgO, SiO_2, CaO and ZnO to model the presence of forsterite. Those calculations assume an elemental activity of 1 thereby giving the highest single partial pressure of the individual molecules (In reality the activity will be lower as the elements are part of a crystal structure). The results display for the individual oxides the highest partial pressures for the formation of the following oxides/hydroxides: La_2O_3 with $3.69 \cdot 10^{-29}$; $Sr(OH)_2$ with $3{,}95 \cdot 10^{-10}$; $Fe(OH)_2$ $5.45 \cdot 10^{-13}$; MnO_2 with $2.00 \cdot 10^{-18}$ bar; $Mg(OH)_2$ with $3.12 \cdot 10^{-13}$ bar; $Si(OH)_4$ with $1.43 \cdot 10^{-08}$ bar; $Ca(OH)_2$ with $2.77 \cdot 10^{-12}$ bar and $Zn(OH)_2$ with $3.24 \cdot 10^{-10}$ bar respectively. Thus $Sr(OH)_2$ for ESC_LSF_pure is the most probable volatile species and $Si(OH)_4$ is the most probable volatile species for the ESC_LSF_mixed cell setup. All other possible gaseous phases are less probable, e.g. have an even lower partial pressure. This is contradictory to Mogensen et al. [6] as the formation of a volatile Mn containing species is relatively unlikely (10 or 8 orders of magnitude less compared to $Si(OH)_4$ and $Sr(OH)_2$, respectively).

Furthermore Pellegrinelli et al. [34] observed on LSCF-GDC model cells two types of degradation behavior: a short-term reversible and a long-term irreversible degradation. The short-term reversible degradation underlines the effect of water: the blocking of the oxygen reduction reaction (ORR) resulting in an instantaneous performance loss. The long-term degradation is related to the enhanced sintering of

LSCF-GDC electrodes caused by H_2O and CO_2. Furthermore CO_2 actively participates at the ORR and occupies a number of surface sites. However the effects reported on CO_2 do not play a role in the present studies. Having the results of Nielsen, Menzler and Pellegrinelli in mind, the results presented here perfectly fit the observed degradation of 3.7 % if a two layer cathode, consisting of LSF electrode and LSM CCL (e.g. Figure 8 (A)) compared to e.g. a full LSM/8YSZ cathode with an overall degradation of 8.4% (Nielsen and Mogensen [6]) is used. As in our cell configuration the LSM acts only as the CCL and not as the active electrode. Furthermore, for the ESC_LSF_mixed cell it seems that the presence of forsterite protects the cell as the observable degradation is with 1.4 % rather small compared to the 3.7 % for the ESC_LSF_pure cell setup. This can be explained by the pathway of the humidified air towards the catalytic active LSF. At first the humidified air passes the LSM CCL, hence, forming the different volatile species $Mn(OH)_2$, $Sr(OH)_2$ and additionally for the cell with forsterite $Si(OH)_4$ related to their single probability (partial vapor pressure). Thereby the humidification level of the air depletes locally for the cell utilizing forsterite within the LSM CCL more water vapor compared to the cell utilizing a pure LSM CCL. This results for the ESC_LSF_mixed in a reduced available water content when the humidified air reaches the catalytic active LSF cathode. Thus the presence of forsterite, serving as Si-source, protects LSF by reducing the amount of water on the way to the cathode (“getter”), hence, resulting in an overall reduced cell degradation if ESC_LSF_pure and ESC_LSF_mixed is compared (3.7 % vs. 1.4 % e.g. Figure 8 (A) and (B)).

b) Co-firing at 1100°C<T<1300°C affects cathode stability in such a way that LSM tends to form Mn-rich phases in the presence of 8YSZ under these manufacturing conditions. [35] Due to the Mn depletion A-site cations maybe more easily released too. Therefore giving easy access to Sr-ions enhancing the formation of volatile oxides if water is present thus explaining the faster degradation which is observed in the present work compared with that reported by Nielsen and Mogensen [6].

5 Conclusion

A cathode material with high-temperature stability, superior catalytic activity and co-firing capability was sought to enable a low-cost ISC to be manufactured. This low-cost ISC utilizes forsterite as the support material, which is applied at the air side of the cell. In Part I of this paper, the reaction tendency with forsterite and the influence on the cathodic microstructure and secondary phase formation was studied. As part of this work, the material perspective was linked to electrocatalytic performance in terms of electrochemical impedance spectroscopy and selected cathodes for single-cell tests. EIS measurements revealed the following order of polarization resistances: LSF < LSM/8YSZ < PSCF < LSFM_95S1M3 < LSFM_95S2M8 < LSCF < LCCF < LSC.

The formation of the insulating $SrZrO_3$ or $Ca_{0.15}Zr_{0.85}O_{1.85}$ phase plays a crucial role and was linked to the respective polarization resistances of each cathode material. LSF only displays an island-like formation of $SrZrO_3$ secondary phase. However, LSC, which represents the least catalytically active material, displays the formation of a thick and continuous $SrZrO_3$ layer. Furthermore, all the cathodes containing cobalt show GDC postdensification since cobalt acts as a sintering aid, resulting in densification of the GDC layer.

The findings show that each material and material combination has to be carefully chosen and adjusted to the specific functional, manufacturing and application requirements. For instance, the electrochemical performance of a cathode material can be strongly influenced by the required processing parameters, e.g. sintering temperature. Therefore, cathode materials such as LSC and LSCF, which usually display good performance, reveal low catalytic activities compared to mid-class cathode materials. such as LSF.

For the preselected LSF cathode material the stoichiometry and the microstructure should now be optimized. Additionally, an in-depth EIS analysis should be done in parallel, taking the whole spectra into account, to fully understand the influence of forsterite, the associated

co-firing manufacturing route and to optimize the cathode with respect to highest performance.

6 Acknowledgments

Yixing Li (FAU Erlangen-Nuremberg - Chair of Energy Process Engineering) is gratefully acknowledged for her support in conducting the single-cell tests. The authors would also like to thank Dr. Volker Nischwitz, Central Institute of Engineering, Electronics and Analytics – Analytics (ZEA-3), Forschungszentrum Jülich, for performing wet chemical analyses. Xiaoyan Yin (IEK-2), Forschungszentrum Jülich, for performing the FactSage calculations. The project “KerSOLife100” (FKZ: 03ET6101) was funded by the Federal Ministry for Economic Affairs and Energy (BMWi).

7 Supplementary data

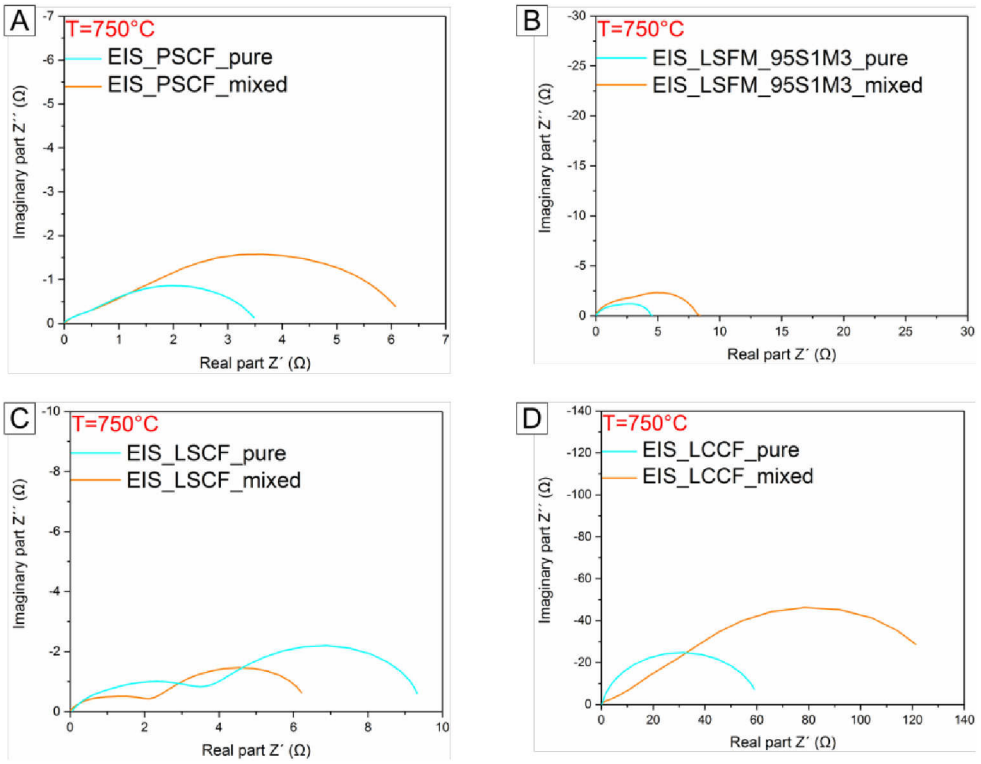

Supplementary 1: Nyquist-plots of the EIS samples with (A) PSCF, (B) LSFM 95S1M3, (C) LSCF and (D) LCCF as cathode material.

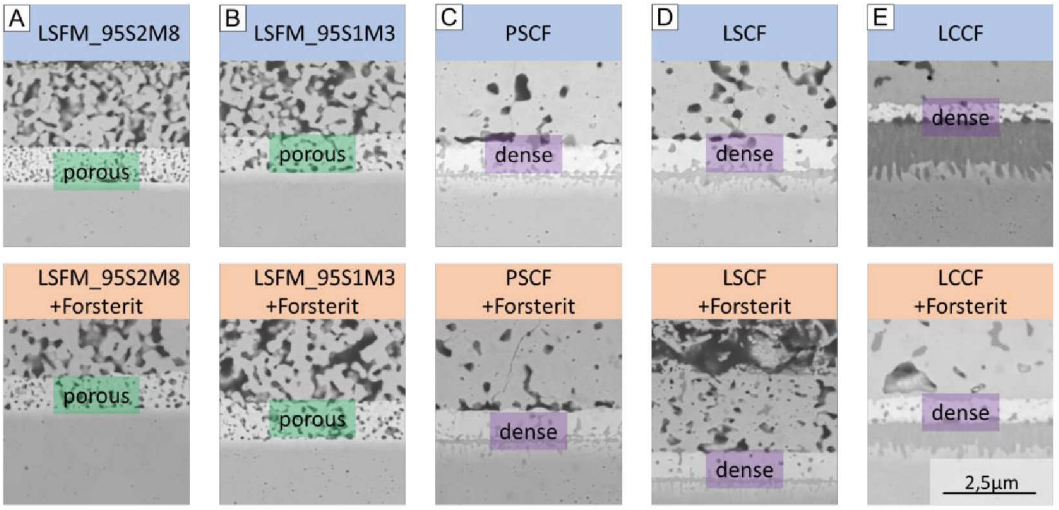

Supplementary 2: GDC densification in a comparison of the nature of the cathode layer for (A) LSFM_95S2M8, (B) LSFM_95S1M3, (C) PSCF, (D) LSCF and (E) LCCF. The GDC layer is marked in green if it is porous and in purple if it is dense.

8 References

[1] H. Takei, T. Kobayashi, Journal of Crystal Growth, 23 (1974) 121-124.
[2] J.M. Andújar, F. Segura, Renewable and Sustainable Energy Reviews, 13 (2009) 2309-2322.
[3] N.Q. Minh, T. Takahashi, Science and Technology of Ceramic Fuel Cells, Elsevier Science Ltd, Oxford, 1995.
[4] C. Lenser, N.H. Menzler, Solid State Ionics, 334 (2019) 70-81.
[5] B.A. Boukamp, Solid State Ionics, 169 (2004) 65-73.
[6] J. Nielsen, M. Mogensen, Solid State Ionics, 189 (2011) 74-81.
[7] A. Leonide, B. Rüger, A. Weber, W.A. Meulenberg, E. Ivers-Tiffée, Journal of The Electrochemical Society, 157 (2010) B234-B239.
[8] N.H.Menzler, J.Malzbender, P.Schoderböck, R.Kauert, H.P.Buchkremer, Fuel Cells, 14 (2014) 96-106.
[9] X. Meng, S. Lü, Y. Ji, T. Wei, Y. Zhang, Journal of Power Sources, 183 (2008) 581-585.
[10] J. Kong, Y. Zhang, C. Deng, J. Xu, Journal of Power Sources, 186 (2009) 485-489.
[11] W. Wang, Y. Huang, S. Jung, J.M. Vohs, R.J. Gorte, Journal of The Electrochemical Society, 153 (2006) A2066-A2070.
[12] W. Wang, M.D. Gross, J.M. Vohs, R.J. Gorte, Journal of The Electrochemical Society, 154 (2007) B439-B445.
[13] Y.-Q. Guo, Y.-M. Yin, Z. Tong, J.-W. Yin, M.-W. Xiong, Z.-F. Ma, Solid State Ionics, 193 (2011) 18-22.
[14] F. Zhao, R. Peng, C. Xia, Fuel Cells Bulletin, 2008 (2008) 12-16.
[15] M.F. Yan, Materials Science and Engineering, 48 (1981) 53-72.
[16] M.C. Verbraeken, T. Ramos, K. Agersted, Q. Ma, C.D. Savaniu, B.R. Sudireddy, J.T.S. Irvine, P. Holtappels, F. Tietz, Rsc Advances, 5 (2015) 1168-1180.
[17] H. Ullmann, N. Trofimenko, F. Tietz, D. Stover, A. Ahmad-Khanlou, Solid State Ionics, 138 (2000) 79-90.
[18] Y.D. Li, J.M. Chen, Y.C. Lee, Journal of Ceramic Processing Research, 19 (2018) 461-466.
[19] F.W. Poulsen, N. Vanderpuil, Solid State Ionics, 53 (1992) 777-783.
[20] V. Wilde, H. Stormer, J. Szasz, F. Wankmuller, E. Ivers-Tiffee, D. Gerthsen, Acs Applied Energy Materials, 1 (2018) 6790-6800.
[21] J. Szász, F. Wankmüller, V. Wilde, H. Störmer, D. Gerthsen, N.H. Menzler, E. Ivers-Tiffée, Journal of The Electrochemical Society, 165 (2018) F898-F906.
[22] E. Jud, C.B. Huwiler, L.J. Gauckler, Journal of the American Ceramic Society, 88 (2005) 3013-3019.
[23] P. Hjalmarsson, M. Søgaard, M. Mogensen, Solid State Ionics, 179 (2008) 1422-1426.
[24] D. Ding, X. Li, S.Y. Lai, K. Gerdes, M. Liu, Energy & Environmental Science, 7 (2014) 552-575.
[25] A. Nechache, M. Cassir, A. Ringuedé, Journal of Power Sources, 258 (2014) 164-181.
[26] M. Dragan, S. Enache, M. Varlam, K. Petrov, Perovskite-Type Lanthanum Cobaltite LaCoO 3: Aspects of Processing Route toward Practical Applications, in: Cobalt Compounds and Applications, IntechOpen, 2019.
[27] M. Mogensen, Ionic and Mixed Conducting Ceramics 6, Electrochemical Society, 2008.
[28] V. Vashuk, L. Kokhanovskii, I. Yushkevich, Inorganic materials, 36 (2000) 79-83.
[29] K. Yashiro, I. Nakano, M. Kuhn, S. Hashimoto, K. Sato, J. Mizusaki, ECS Transactions, 35 (2011) 1899-1907.
[30] C. Niedrig, S.F. Wagner, W. Menesklou, E. Ivers-Tiffée, Solid State Ionics, 273 (2015) 41-45.
[31] J. Nielsen, A. Hagen, Y.L. Liu, Solid State Ionics, 181 (2010) 517-524.
[32] H. Yokokawa, H.Y. Tu, B. Iwanschitz, A. Mai, Journal of Power Sources, 182 (2008) 400-412.

[33] N.H. Menzler, P. Batfalsky, A. Beez, L. Blum, S. Groß-Barsnick, L. Niewolak, W. J. Quadakkers, R. Vaßen, in: 12th European SOFC & SOE Forum 2016, Lucerne/Switzerland, 2016, pp. 290-297.
[34] C. Pellegrinelli, Y.-L. Huang, E.D. Wachsman, ECS Transactions, 91 (2019) 665-680.
[35] E. Matte, G. Holzlechner, L. Epple, D. Stolten, P. Lupetin, Journal of Power Sources, 413 (2019) 334-343.